## Journal of Materials Chemistry A



PAPER

View Article Online
View Journal | View Issue



Cite this: J. Mater. Chem. A, 2018, 6, 13806

Received 12th April 2018 Accepted 23rd June 2018

DOI: 10.1039/c8ta03344g

rsc.li/materials-a

# Investigation of n-type doping strategies for Mg<sub>3</sub>Sb<sub>2</sub>†

Prashun Gorai, \*\*D\*\*\* Brenden R. Ortiz, \*\*D\*\* Eric S. Toberer \*\*D\*\* and Vladan Stevanović\*\*\*

Recent, and somewhat surprising, successful n-type doping of  $Mg_3Sb_2$  was the key to realizing high thermoelectric performance in this material. Herein, we use first-principles defect calculations to investigate different extrinsic n-type doping strategies for  $Mg_3Sb_2$  and to reveal general chemical trends in terms of dopant solubilities and maximal achievable electron concentrations. In agreement with experiments, we find that Sb substitution is an effective doping strategy, with Se and Te doping predicted to yield up to  $\sim 8 \times 10^{19}$  cm<sup>-3</sup> electrons. However, we also find that Mg substitution with trivalent (or higher) cations can be even more effective; in particular, the predicted highest achievable electron concentration ( $\sim 5 \times 10^{20}$  cm<sup>-3</sup>) with La as an extrinsic dopant exceeds that of Se and Te doping. Interstitial doping (Li, Zn, Cu, Be) is found to be largely ineffective either due to self-compensation (Li) or high formation energy (Zn, Cu, Be). Our results offer La as an alternative dopant to Te and Se and reinforce the need for careful phase boundary mapping in achieving high electron concentrations in  $Mg_3Sb_2$ .

## 1 Introduction

Intrinsic and extrinsic point defects play a critical role in determining properties of semiconductors including their dopability *i.e.* the achievable concentrations of free charge carriers of a certain type (electrons or holes). The dopability of a semiconductor is largely determined by the presence of native (intrinsic) defects and/or the properties of extrinsic dopants such as their solubilities at the growth conditions as well as their electronic properties.

In thermoelectrics, the concentrations of charge carriers needed to optimize the thermoelectric figure of merit, zT, are typically high ( $10^{19}$  to  $10^{20}$  cm $^{-3}$ ). Therefore, understanding dopability is crucial to realize the full potential of thermoelectric materials. A prominent example of how native defects and growth conditions influence the dopability of materials and their thermoelectric performance is  $Mg_3Sb_2$  (Fig. 1). Historically,  $Mg_3Sb_2$  was almost exclusively synthesized as a p-type material with a modest zT in the 0.2–0.4 range. The main reason is the high volatility of Mg, which typically results in Mg-poor samples with significant concentrations of acceptor Mg vacancies. More recently, n-type  $Mg_3Sb_2$  was synthesized with excess Mg i.e., under Mg-rich growth conditions, which suppresses the formation of Mg vacancies, thereby resulting

in relatively low intrinsic n-type doping. More importantly, this allows further enhancement of electron concentrations through extrinsic doping with Se and Te. Together with Bi alloying to

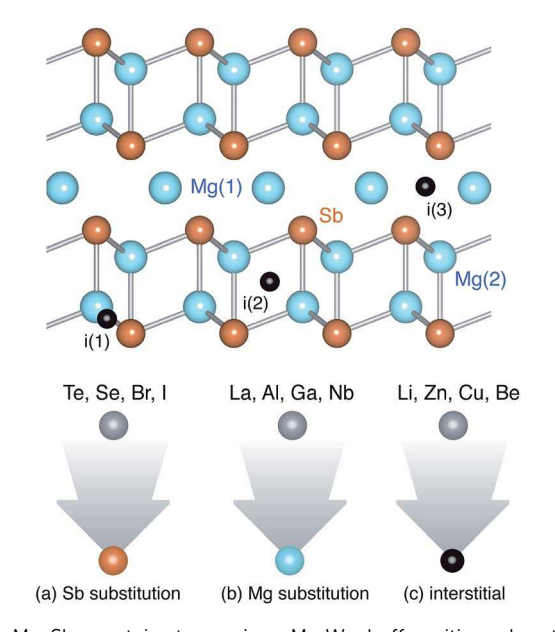


Fig. 1  $Mg_3Sb_2$  contains two unique Mg Wyckoff positions denoted by Mg(1) and Mg(2), and one unique Sb Wyckoff position. Favorable interstitial sites are marked by black spheres and denoted by i(1), i(2), and i(3). The crystal structure of  $Mg_3Sb_2$  can be visualized as slabs of  $[Mg_2Sb_2]^{2-}$  slabs intercalated with  $Mg^{2+}$  cations. Strategies for n-type doping include: (a) Sb substitution with mono- (Br, I) or di-valent (Se, Te) anions, (b) Mg substitution with tri- or higher-valent cations (La, Al, Ga, Nb), and (c) insertion of cation interstitials (Li, Zn, Cu, Be).

<sup>&</sup>quot;Colorado School of Mines, Golden, CO 80401, USA. E-mail: pgorai@mines.edu; vstevano@mines.edu

<sup>&</sup>lt;sup>b</sup>National Renewable Energy Laboratory, Golden, CO 80401, USA

<sup>†</sup> Electronic supplementary information (ESI) available. See DOI: 10.1039/c8ta03344g

reduce the lattice thermal conductivity, n-type  $Mg_3Sb_2$  has demonstrated a high zT > 1.5. The experimental reports of high zT were preceded by computational predictions of promising thermoelectric performance of  $Mg_3Sb_2$  for the assumed n-type doping. The good thermoelectric performance is attributed to the large number of carrier pockets (high band degeneracy) and small band effective masses in the conduction band, which result in high electrical conductivity and large Seebeck coefficient for electrons.

Using modern, first-principles defect calculations, we have previously investigated the role of native defects and growth conditions in the dopability of Mg<sub>3</sub>Sb<sub>2</sub> and contributed to the understanding of the effectiveness of n-type doping with Te.6 We found that the predominant defect changes from Mg vacancies under Mg-poor conditions to Mg interstitials under Mg-rich conditions; consequently, Mg<sub>3</sub>Sb<sub>2</sub> changes its selfdoping behavior from p-type to n-type. More importantly, the absence of Mg vacancies under Mg-rich conditions allows effective (uncompensated) extrinsic n-type doping with Te, and achievable free electron concentrations in excess of 10<sup>19</sup> cm<sup>-3</sup>. We revisit these prior findings in more detail in Section 3. While chalcogens (Se, Te) have been demonstrated to be effective ntype dopants, the doping behavior of other possible extrinsic n-type dopants and doping strategies beyond Sb substitution have not been explored so far.

In this study, we move beyond Te and use modern defect theory and defect calculations to investigate and compare various extrinsic n-type doping strategies for Mg<sub>3</sub>Sb<sub>2</sub> including Sb substitution, Mg substitution and interstitial doping as illustrated in Fig. 1. Additionally, we reveal general chemical trends for the various dopants, in terms of their solubilities and maximal achievable electron concentrations. The computational approach adopted in this work combines the supercell method with finite size corrections and band edge shifts from GW calculations,11 which has been demonstrated to provide reliable predictions of the energetics of native and extrinsic defects in semiconductors and the resulting charge carrier concentrations. In spite of its seemingly simple binary chemistry, the predicted carrier concentrations exhibit surprisingly complex behavior due to the presence of charge compensating defects and competing phases.

In total, we consider 11 extrinsic dopants following the three strategies: (1) Sb substitution - Se, Br, and I, (2) Mg substitution - La, Al, Ga, and Nb, and (3) interstitial insertion - Li, Zn, Cu, and Be. Our study reveals that, of all the dopants considered, La is the most effective extrinsic n-type dopant in Mg<sub>3</sub>Sb<sub>2</sub>, and Mg substitution the most effective doping strategy. Mg substitution is even more effective than Sb substitution with Se and Te. The predicted maximal achievable electron concentrations for La doping ( $\sim 5 \times 10^{20} \text{ cm}^{-3}$  at 900 K) are almost an order of magnitude higher than that achieved with Te or Se doping. Other group-III elements (Al and Ga) are not as effective due to the counterintuitive self-compensation from dopant substitution of Sb. We also find Nb to be largely ineffective, which contradicts recent reports of Nb-doped Mg<sub>3</sub>Sb<sub>2</sub>. Interstitial doping (Li, Zn, Cu, Be) is ineffective, either due to selfcompensation (Li) or high formation energy of the interstitials

(Zn, Cu, Be). Our results further support the need for careful phase boundary mapping<sup>6</sup> in the dopant-Mg–Sb chemical potential phase space; for some dopants, due to the counterintuitive role of charge compensating defects, the maximal free electron concentration may be achieved under less Mg-rich growth conditions. Finally, while this study is limited to n-type doping of Mg<sub>3</sub>Sb<sub>2</sub>, the general principle of dopant phase boundary mapping can be extended to doping of other materials.

## 2 Methods

#### 2.1 Calculation of defect energetics

To calculate the energetics of native point defects and extrinsic dopants in  $Mg_3Sb_2$ , we perform first-principles defect calculations with density functional theory (DFT). Eqn (1) describes how the formation energy ( $\Delta H_{D,q}$ ) of a point defect D in charge state q is calculated:

$$\Delta H_{\rm D,q} = \left(E_{\rm D,q} - E_{\rm H}\right) + \sum_{i} n_i \mu_i + q E_{\rm F} + E_{\rm corr} \tag{1}$$

The term  $E_{D,q} - E_H$  represents the difference in the total energy of the defect-free host crystal with no net charge  $(E_H)$  and the host crystal with defect D in charge state q. The terms  $\sum_i n_i \mu_i$ 

and  $qE_F$  account for the energy associated with exchange of elemental species and charge, respectively. The chemical potential of element i is denoted by  $\mu_i$  and  $n_i$  is the number of atoms of element i added  $(n_i < 0)$  or removed  $(n_i > 0)$  to form the defect D.  $E_F$  is the Fermi energy. First-principles defect calculations are typically performed using periodically-repeated supercells, an approach that suffers from the artifacts arising from finite size effects. Additional artifacts arise from the limitations of the first-principles method e.g. underestimation of the band gap with standard functionals used in DFT. Various corrections to the defect formation energy are applied to alleviate these artifacts. These corrections are grouped into the  $E_{\rm corr}$  term and briefly discussed in the following paragraphs. A more detailed description can be found elsewhere.  $^{12}$ 

To calculate the total energies of the supercells, the generalized gradient approximation of Perdew–Burke–Ernzerhof (PBE)<sup>13</sup> is utilized in the projector augmented wave (PAW) formalism as implemented in the VASP software package.<sup>14</sup> The defect energetics are calculated using the standard supercell approach.<sup>12</sup> The total energies of defect supercells containing 90 atoms are calculated with a plane-wave energy cutoff of 340 eV and a  $\Gamma$ -centered Monkhorst pack k-point grid to sample the Brillouin zone. The defect supercells are relaxed following the procedure used in ref. 15.

The elemental chemical potential  $\mu_i$  can be expressed relative to the reference elemental phase as  $\mu_i = \mu_i^0 + \Delta \mu_i$ , where  $\mu_i^0$  is the reference chemical potential under standard conditions and  $\Delta \mu_i$  is the deviation from the reference chemical potential.  $\Delta \mu_i = 0$  corresponds to *i*-rich conditions. Inspired by the FERE approach, <sup>16</sup> the reference chemical potentials  $(\mu_i^0)$  are established for elements in a family of materials (*e.g.* Mg–Sb, Mg–Sb–

Te, Mg-Sb-Br) by fitting to a set of measured formation enthalpies of compounds in that material family. The bounds on  $\Delta \mu_i$  for a given compound is set by the region of phase stability.

The underestimation of band gap in DFT is rectified by applying band edge shifts as determined from GW quasiparticle energy calculations. The following corrections are included in  $E_{\rm corr}$ , following the methodology outlined in ref. 12: (1) image charge correction for charge defects, (2) potential alignment correction for charged defects, (3) band filling correction for shallow defects, and (4) band gap correction for shallow acceptors/donors. The calculation setup and analyses are performed using a software package for automation of point defect calculations.<sup>17</sup>

Defect enthalpies of all vacancies, antisites, and interstitials in charge states q = -3, -2, -1, 0, 1, 2, and 3 are calculated. Vacancies and antisites derived from all unique Wyckoff positions in the crystal structure are considered in the calculations. Likely interstitial sites are identified by Voronoi tessellation as implemented in the software package.17 The position of the equilibrium Fermi energy, the corresponding defect concentrations, and the free carrier concentrations at a given temperature are calculated self-consistently by establishing the charge neutrality condition. The defect concentrations are calculated using the rigid band approximation, which is valid when the dopant concentrations are low such that the electronic structure, to a first approximation, remains unperturbed by doping. For effective dopants, the dopant concentrations are typically low and the rigid band approximation is likely to be valid, as demonstrated for Te doping of Mg<sub>3</sub>Sb<sub>2</sub>.6

#### 2.2 Synthesis and doping

Mg<sub>3</sub>Sb<sub>2</sub> and Li-doped Mg<sub>3</sub>Sb<sub>2</sub> were synthesized under Mg-rich conditions, from Mg shavings (Alfa 99.9%), Sb shot (Alfa 99.999%), and Li rod (99.8%). All sample preparations were performed in an argon glove box with oxygen and water concentrations < 1 ppm. Mg shavings were purified by immersion in a solution of 200 mL reagent-grade anhydrous ethanol and 4 mL of concentrated HCl for 2 min, followed by a ethanol rinse and drying *en vacuo*. Elements were loaded into tungsten carbide ball mill vials with 3/4'' tungsten carbide balls and milled for 2 h. Resulting powders were ground and sieved through a 106 μm mesh and densified *via* reactive hot-pressing under vacuum (<2 mTorr) at 600 °C.

## 3 Prior findings

We have previously investigated the role of native defects and growth conditions in the dopability of Mg<sub>3</sub>Sb<sub>2</sub> and predicted effective n-type doping with Te.<sup>6</sup> In this section, we revisit those prior findings for the purposes of contextualizing the results of various n-type doping strategies investigated in this work.

#### 3.1 Self doping

Native defects can result in self doping, as in the case of LiZnSb and SnSe. The calculated formation energies of native defects as

a function of the Fermi energy  $(E_{\rm F})$  in Mg<sub>3</sub>Sb<sub>2</sub> are shown in Fig. 2 under Mg-poor and Mg-rich growth conditions (figures modified from ref. 6). Defects with plots that have positive slopes are donors and negative slopes are acceptors. Neutral defects with zero slopes do not participate in the overall charge balance. Mg vacancies are the only acceptors in Mg<sub>3</sub>Sb<sub>2</sub> while all of the other native defects are donors. The lowest energy configuration of the Mg interstitial is found to be in the octahedral site denoted by i(2) in Fig. 1 while the Sb interstitial in the tetrahedral site denoted by i(1). Mg<sub>3</sub>Sb<sub>2</sub> has no other binary competing phases; consequently, the limit of Mg-poor condition corresponds to equilibrium with Sb ( $\Delta\mu_{Sb} = 0$  eV) and Mg-rich condition to equilibrium with Mg ( $\Delta \mu_{\text{Mg}} = 0$  eV). Due to the inherent volatility of Mg, historically, Mg<sub>3</sub>Sb<sub>2</sub> has been grown under Mg-poor conditions, where the material is p-type. However, our recent work on phase boundary mapping shows that Mg<sub>3</sub>Sb<sub>2</sub> is n-type when grown under Mg-rich conditions.

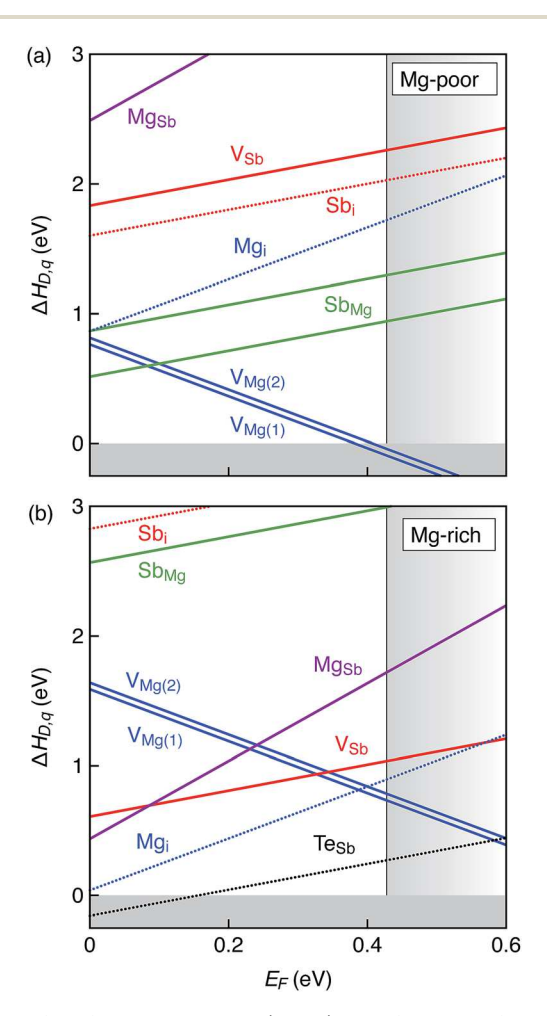


Fig. 2 Defect formation energy ( $\Delta H_{\rm D,q}$ ) as a function of the Fermi energy ( $E_{\rm F}$ ) for Mg<sub>3</sub>Sb<sub>2</sub> grown under (a) Mg-poor and (b) Mg-rich conditions.  $E_{\rm F}$  is referenced to the valence band edge. The shaded region on the right represents the conduction band. Under Mg-poor conditions, Mg<sub>3</sub>Sb<sub>2</sub> is p-type while under Mg-rich conditions, Mg<sub>3</sub>Sb<sub>2</sub> is n-type. Formation energy of substitutional Te<sub>Sb</sub> under Mg-rich conditions is also shown in (b), where Te is an effective n-type extrinsic dopant.

Mg-poor conditions. Under Mg-poor growth conditions, Mg vacancies are the dominant native defects (Fig. 2a), a common trait of the 1-2-2 phases.18 For Mg3Sb2 grown at 900 K, the concentration of the acceptor defect  $V_{Mg}^{2-}$  is  $\sim 6.7 \times 10^{18}$  cm<sup>-3</sup>. We found that the donor antisite  $Sb_{Mg(1)}$  is also the dominant defect under Mg-poor conditions with  $Sb_{Mg(1)}^{1+}$  concentration of  $\sim$ 7.0  $\times$  10<sup>18</sup> cm<sup>-3</sup> (900 K). As a result of charge compensation between the donor V<sub>Mg</sub> and acceptor Sb<sub>Mg(1)</sub>, Mg<sub>3</sub>Sb<sub>2</sub> is moderately p-type with hole concentration  $\sim$ 6.4  $\times$  10<sup>18</sup> cm<sup>-3</sup> at 900 K. The predicted hole concentration is in fairly good agreement with experimental measurements.3-5 Within thermoelectrics, cation vacancies are well known as "electron killers" because they act as acceptors and limit the n-type dopability of materials, particularly in Zintl compounds such as ZnSb, 19 and Ca<sub>5</sub>Al<sub>2</sub>Sb<sub>6</sub>. 20 The presence of large concentrations of Mg vacancies in Mg<sub>3</sub>Sb<sub>2</sub> has been previously recognized.<sup>18</sup>

Mg-rich conditions. Under Mg-rich conditions, Mg interstitials are the dominant defects (Fig. 2b) such that the  $E_{\rm F}$  is pinned above the mid-gap and Mg<sub>3</sub>Sb<sub>2</sub> is n-type. Sb vacancies (V<sub>Sb</sub>) are also present in appreciable concentrations. For instance, at 900 K growth temperature, the concentrations of Mg<sub>i</sub> and V<sub>sh</sub> are 1.9  $\times$  10  $^{18}$  cm  $^{-3}$  and 1.2  $\times$  10  $^{17}$  cm  $^{-3}$ , respectively. At the same temperature, the concentration of Mg vacancies is of the order of 10<sup>16</sup> cm<sup>-3</sup>. The predicted free electron concentration of  $3.8 \times 10^{18} \text{ cm}^{-3}$  was found to be in good agreement with the measurements reported in the literature for samples grown with excess Mg.6 Our results suggested that in Mg3Sb2 grown under Mg-rich conditions, Mg interstitials are indeed responsible for the n-type behavior.

In our prior study,6 we concluded that under Mg-poor conditions, it is not possible to extrinsically dope Mg<sub>3</sub>Sb<sub>2</sub> with large concentrations of electrons because of charge compensation with acceptor Mg vacancies. Under Mg-rich conditions (Fig. 2b), the formation energy of Mg vacancies at the conduction band minima is ~0.8 eV. Therefore, Mg₃Sb₂ can be further extrinsically doped with electrons provided the formation energy of the donor dopant is lower than ~0.8 eV at the conduction band minima.

#### 3.2 Extrinsic doping: tellurium

The defect formation energy of the substitutional donor defect Tesb is shown in Fig. 2(b), which is lower than that of Mg interstitial. We found that the Fermi energy is pinned inside the conduction band, resulting in degenerate n-type doping with  $\sim 4 \times 10^{19} \text{ cm}^{-3}$  electrons (900 K), and in excellent agreement with our experimental measurements of Te-doping.6 Unlike undoped Mg<sub>3</sub>Sb<sub>2</sub> grown under Mg-rich conditions where Mg interstitials are the dominant defects, in Te-doped Mg<sub>3</sub>Sb<sub>2</sub> Mg interstitials are present is very low concentrations and do not play a role in n-type doping; in fact, the concentration of Mg vacancies exceed that of Mg interstitials.

#### Results

As described in the Introduction, the different n-type doping strategies (Fig. 1) for Mg<sub>3</sub>Sb<sub>2</sub> can be broadly classified into (a)

anion substitution, (b) cation substitution, and (c) interstitial insertion. In this section, we computationally investigate a diverse set of 11 extrinsic dopants spanning the three different doping strategies. We consider 3 anion substitutions (Se, Br, I), 4 cation substitutions (La, Al, Ga, Nb), and 4 interstitial insertions (Li, Zn, Cu, Be). For each of these extrinsic dopants, the defect energetics are presented under Mg-rich conditions only (Fig. 3-5). The defect energetics of Nb and Be doping can be found in the ESI.†

#### 4.1 Anion substitution

Anion substitution (Fig. 1a) is the most common strategy that has been adopted for extrinsic n-type doping of  $Mg_3Sb_2$ . The substituting anion must be di- or mono-valent since Sb is trivalent. Here, we consider di-valent chalcogenide (Se) and mono-valent halides (Br, I) as potential n-type dopants. In our 0, 1, 2, 3) of the defect. The defect plots corresponding to each of these dopants are presented in Fig. 3 for Mg-rich and the most extrinsic dopant-rich conditions as allowed by the phase stability of Mg<sub>3</sub>Sb<sub>2</sub> in the ternary Mg-Sb-dopant phase space.

Selenium. The defect plot corresponding to the substitutional Sesb is shown in Fig. 3. The formation energy of the donor Sesb is lower than that of Mg interstitials. As a result, the Fermi energy  $(E_F)$  is pinned inside the conduction band (shaded region on the right in Fig. 3). Therefore, Se should be an effective n-type dopant that degenerately dopes Mg<sub>3</sub>Sb<sub>2</sub> under Mg-rich conditions. The maximal free electron concentration is achieved under Mg-rich and the most dopant-rich conditions accommodated by the phase stability of Mg<sub>3</sub>Sb<sub>2</sub> in the Se-Mg-Sb ternary phase space (Section 5). Indeed, Se has been

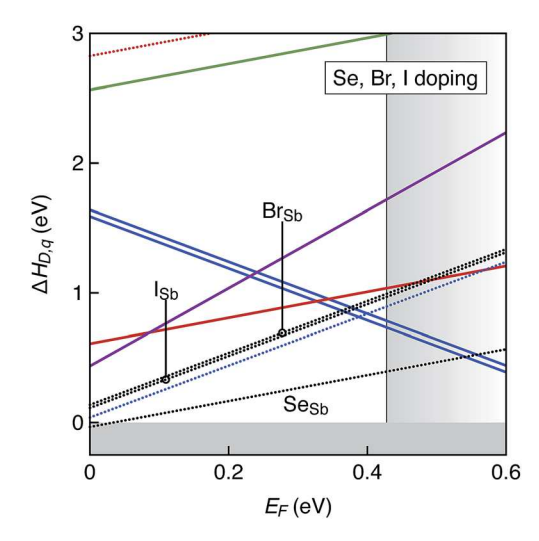


Fig. 3 Defect energetics of n-type doping of Mg<sub>3</sub>Sb<sub>2</sub> by anion substitution under Mg-rich and most dopant-rich conditions. The native defects (Fig. 2) are also shown for reference. Doping with chalcogenides (Se) and halides (Br, I). Substitutional Se<sub>Sb</sub>, denoted by black dotted line, acts as an effective n-type dopant with formation energy lower than that of Mg interstitials. Substitutional halide dopants (Br<sub>Sb</sub>, I<sub>Sb</sub>), denoted by black dotted lines, exhibit formation energies similar to Mgi and are not effective n-type dopants.

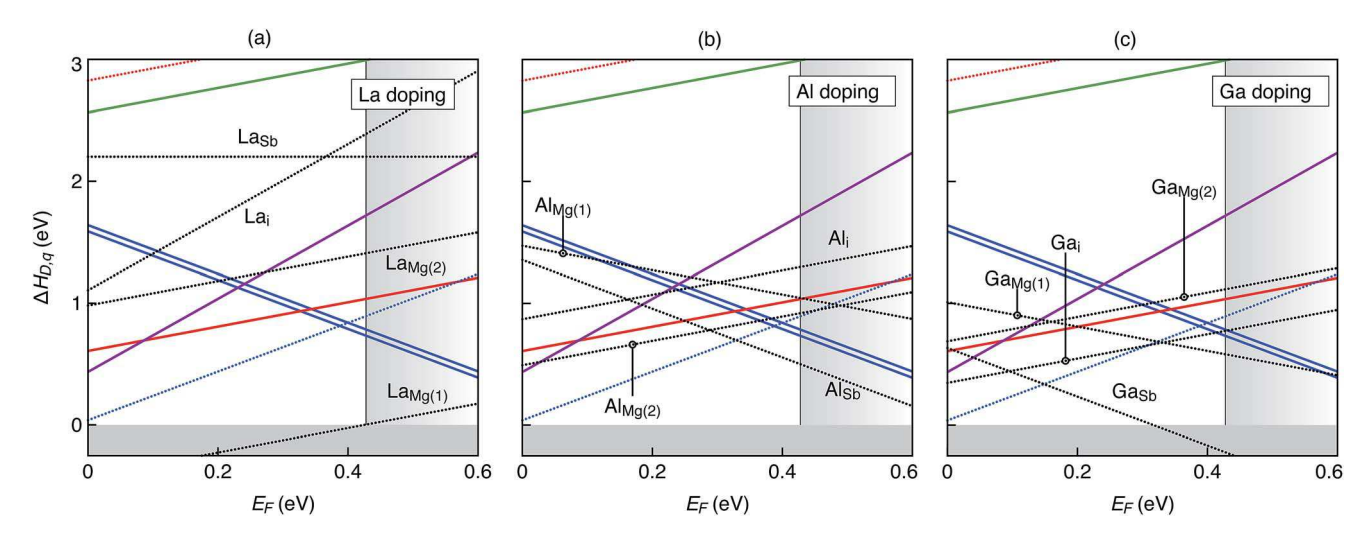


Fig. 4 Defect energetics of n-type doping of  $Mg_3Sb_2$  by cation substitution under Mg-rich ( $\Delta\mu_{Mq}=0$  eV) and most dopant-rich conditions. The native defects (Fig. 2) are also shown for reference. Doping with (a) La, (b) Al, (c) Ga. The defects corresponding to the extrinsic dopants are denoted by black dotted lines. La is found be an effective dopant with predicted electron concentrations in excess of 10<sup>20</sup> cm<sup>-3</sup> (900 K) while Al and Ga are ineffective due to electron compensation by dopant substitution of Sb. The low formation energy of Gash renders Mg<sub>3</sub>Sb<sub>2</sub> p-type under Mg- and Ga-rich conditions.

experimentally found to be a good n-type dopant; Se-doped Mg<sub>3</sub>Sb<sub>2</sub> exhibits relatively high zT of 1.23. The predicted electron concentration of  $4 \times 10^{19} \text{ cm}^{-3}$  at 900 K is in fairly good agreement with measurements, which provides further confidence in the fidelity of the first-principles defect calculations. When  $E_{\rm F}$  is pinned inside the conduction band, the formation energy of Mg vacancies is lower than that of Mg interstitials. The concentration of Mg vacancies far exceeds Mg interstitials in Sedoped Mg<sub>3</sub>Sb<sub>2</sub>, similar to our findings for Te-doped Mg<sub>3</sub>Sb<sub>2</sub> in our prior work.

**Bromine**, iodine. Substitutional doping of the anion (Sb) site in Mg<sub>3</sub>Sb<sub>2</sub> with monovalent anions such as halides has the distinct advantage that, in principle, for every halide ion two free electrons are generated when the halide is fully ionized. Compared to that, divalent chalcogenides can generate only one electron per chalcogenide ion. The disadvantage is that the formation energy ( $\Delta H_{\rm D,q}$ ) as a function of the Fermi energy ( $E_{\rm F}$ ) increases with a slope of 2 as compared to a slope of unity for chalcogens (eqn (1)). The substitutional Br<sub>Sb</sub> is a donor defect, as shown in Fig. 3a, with formation energy that is comparable to that of Mg interstitials under Mg-rich growth conditions. As a result, the free electron concentration is only slightly enhanced by Br doping. The maximal free electron concentration of  $4.4 \times 10^{18} \, \mathrm{cm}^{-3}$  at 900 K is achieved under Mg-rich and most Br-rich conditions allowed by the phase stability of Mg<sub>3</sub>Sb<sub>2</sub> (Section 5). The doping behavior of the substitutional I<sub>Sb</sub> is almost identical to that of Brsb, with maximal free electron concentration of 4.6  $\times$  10<sup>18</sup> cm<sup>-3</sup> at 900 K.

The ineffectiveness of Br and I doping can be partly attributed to the high stability of the competing phases MgBr2 and MgI<sub>2</sub>, which limits the solubility of Br and I in Mg<sub>3</sub>Sb<sub>2</sub>. This is in contrast to Te and Se doping; despite the presence of stable competing phases of Mg chalcogenides (MgTe, MgSe), the

energetics of Sb substitution are far more favorable. As a result, Te and Se are still effective n-type dopants.

#### 4.2 Cation substitution

Mg substitution with a tri- or tetra-valent cation could dope Mg<sub>3</sub>Sb<sub>2</sub> n-type. Here, we consider La, Al and Ga as potential donor dopants. Recent reports of n-type doping with transition metals21,22 such as Nb, Hf, Ta, Co, and Fe prompted us to also consider Nb doping. The defect plots corresponding to each of these dopants are presented in Fig. 4 for Mg-rich and most dopant-rich conditions as accommodated by the phase stability of Mg<sub>3</sub>Sb<sub>2</sub> in the ternary Mg-Sb-dopant phase space.

Lanthanum. The defect energetics of La doping, shown in Fig. 4a, suggests that La is an even more effective n-type dopant compared to Se and Te. As illustrated in Fig. 1, there are two unique Wyckoff positions for Mg atoms in Mg<sub>3</sub>Sb<sub>2</sub>: Mg(1) is the Mg located between the slabs and Mg(2) is the Mg that resides within the Mg<sub>2</sub>Sb<sub>2</sub> slab. La preferentially substitutes Mg(1) over Mg(2); substitutional  $La_{Mg(1)}$  is a low formation energy donor while La<sub>Mg(2)</sub> has significantly higher formation energy. The preferential La substitution of Mg(1) may be attributed to the large ionic size of La<sup>3+</sup> that can be spatially accommodated between the Mg<sub>2</sub>Sb<sub>2</sub> slabs rather than inside the slab by substituting Mg(2). The predicted free electron concentration at 900 K (see Section 5) under Mg-rich and most La-rich conditions is  $4 \times 10^{20}$  cm<sup>-3</sup>, which is higher than that achieved by Se and Te doping. Several competing phases are present in the Mg-Sb-La phase space (Section 5) that limit the most dopant-rich conditions. In spite of the limitations of the dopant-rich conditions, similar to Se and Te doping, La is still an effective n-type dopant. We must note that the stability analysis (see Section 5) in the La-Mg-Sb chemical potential phase space does not take into account off-stoichiometric phases such as La<sub>4</sub>-Mg<sub>4,5</sub>Sb<sub>7</sub>, La<sub>3</sub>Mg<sub>4,6</sub>Sb<sub>6</sub>, and La<sub>4,8,9</sub>Mg<sub>1,66</sub>Sb<sub>6</sub>. These Sb-rich off-

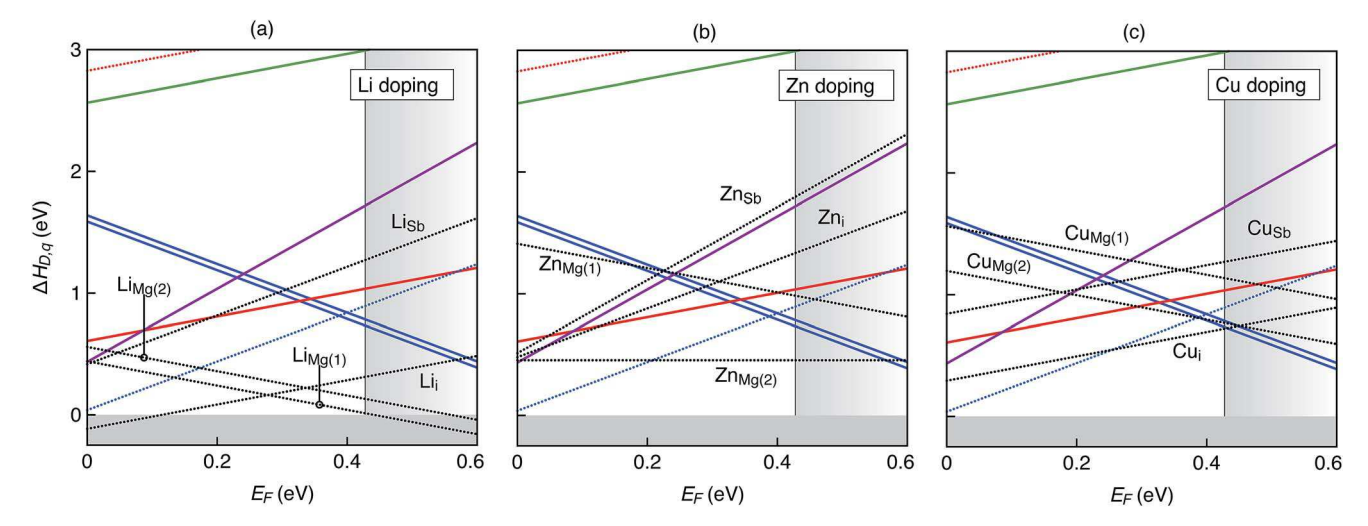


Fig. 5 Defect energetics of n-type doping of  $Mg_3Sb_2$  by interstitial insertion under Mg-rich conditions. The native defects (Fig. 2) are also shown for reference. Doping with (a) Li, (b) Zn, and (c) Cu. The defects corresponding to the extrinsic dopants are denoted by black dotted lines. While Li interstitials have low formation energy, the electrons are compensated by holes created by the acceptor  $Li_{Mg}$ , which also have low formation energy. Zn interstitials have high formation energy and therefore, not effective n-type dopant. Cu interstitials lead to a small increase in the electron concentration.

stoichiometric compounds are likely to form under Sb-rich conditions. However, the maximal achievable electron concentrations occur under Mg-rich conditions (see Section 5) and therefore, the exclusion of these off-stoichiometric phases will not affect the predicted maximal electron concentrations.

While Se and Te are demonstrably successful anion-site dopants, our prediction that La is a highly effective dopant provides a new cation-site dopant. Besides the higher free electron concentration that can be achieved with La doping, there may be additional benefits such as the lowering of the lattice thermal conductivity. It is known from phonon calculations<sup>23</sup> that the low-frequency optical modes ( $\sim$ 3–4 THz) in Mg<sub>3</sub>Sb<sub>2</sub> are dominated by Mg(1) while the higher frequency optical modes ( $\sim$ 6–8 THz) are dominated by Mg(2). Preferential La substitution of Mg(1) combined with the pronounced Mg–La size and mass contrast can provide a source for significant point-defect scattering of the low-frequency optical modes. Given the effectiveness of La as a cation site n-type dopant, Sc and Y can also be expected to be effective dopants.

Aluminum, gallium. Fig. 4b presents the formation energy of defects resulting from Al doping of  $Mg_3Sb_2$  under Mg-rich  $(\Delta\mu_{Mg}=0~eV)$  and Al-rich  $(\Delta\mu_{A1}=0~eV)$  conditions. Several defects are considered, as Al could conceivably substitute Mg and Sb as well as occupy interstitial sites. As expected, substitutional  $Al_{Mg(2)}$  is a donor defect. However, the formation energy of  $Al_{Mg(2)}$  at the conduction band minima is the same as  $Mg_i$  ( $\sim$ 0.8 eV). Substitutional  $Al_{Mg(1)}$  acts as an acceptor, which is contrary to our expectation. The different doping behavior of  $Al_{Mg(1)}$  and  $Al_{Mg(1)}$  is most likely related to the different ionicities of Mg(1) and Mg(2) as proposed in the literature. Nevertheless, the doping behavior of  $Al_{Mg(1)}$  is inconsequential because of its high formation energy. More importantly, the low formation energy of the acceptor defect  $Al_{Sb}$  results in strong charge compensation, resulting in a slight decrease in the free electron

concentration under Mg-rich and Al-rich conditions. For 900 K growth temperature, the free electron concentration in Al-doped Mg\_3Sb\_2 is  $3.3 \times 10^{18}$  cm $^{-3}$ , compared to  $3.8 \times 10^{18}$  cm $^{-3}$  in self-doped Mg\_3Sb\_2. The charge compensation by Al\_Sb can be partly suppressed under Mg-poor (Sb-rich) conditions. As a result, the maximal achievable electron concentration at 900 K is  $7 \times 10^{18}$  cm $^{-3}$  (see Section 5). Al doping can lead to an increase in the electron concentration by a factor of only 2 compared to self-doping. Therefore, Al is not an effective n-type dopant.

The doping behavior of individual defects  $(Ga_{Mg(1)}, Ga_{Mg(2)}, Ga_{Sb}, Ga_i)$  in Ga-doped  $Mg_3Sb_2$  (Fig. 4c) is qualitatively similar to those in Al-doped  $Mg_3Sb_2$ . Surprisingly, the acceptor defect  $Ga_{Sb}$  has a particularly low formation energy resulting in strong charge (electron) compensation. In fact, under Mg-rich ( $\Delta\mu_{Mg}=0$  eV) and Ga-rich ( $\Delta\mu_{Ga}=0$  eV) conditions, the equilibrium Fermi energy is below the mid-gap and  $Mg_3Sb_2$  is doped p-type (Fig. 4c). As in the case of Al doping, the charge compensation due to  $Ga_{Sb}$  may be suppressed under Mg-poor (Sb-rich) conditions, such that  $Mg_3Sb_2$  is doped n-type, albeit with a decreased electron concentration compared to self-doping. The maximal achievable electron concentration is  $2.6 \times 10^{18}$  cm<sup>-3</sup> at 900 K (see Section 5).

**Niobium.** There are recent report of n-type doping of  $Mg_3Sb_2$  with transition metals such as Nb, Hf, Ta, Co, and Fe.<sup>21,22</sup> Within thermoelectrics, the use of transition metals as dopants is unusual and therefore, interesting. Transition metals often exhibit multiple oxidation states that could complicate doping. Consequently, the thermoelectrics community has generally avoided the use of these elements as dopants. Intrigued by the recent reports of n-type doping of  $Mg_3Sb_2$  with Nb, we computationally investigate its doping behavior. The defect energetics of Nb doping are shown in Fig. S1 (ESI†) corresponding to  $Mg_7Sb_2$  in  $Mg_7Sb_2$  and most Nb-rich ( $Mg_7Sb_2$ ) and most Nb-rich ( $Mg_7Sb_2$ ). It is well

know that transition metals such as Nb can exhibit different oxidation states, which is reflected in the different charge states adopted by the substitutional  $\mathrm{Nb_{Mg(1)}}$  (neutral) and  $\mathrm{Nb_{Mg(2)}}$  (singly-charged donor). We find that both  $\mathrm{Nb_{Mg(1)}}$  and  $\mathrm{Nb_{Mg(2)}}$  have high formation energy. Our predictions suggest that Nb is not an effective n-type dopant, which is at odds with recent reports of Nb-doped n-type  $\mathrm{Mg_3Sb_2}$ . In light of these predictions, it would be prudent to revisit the hypotheses proposed in these recent studies.

#### 4.3 Cation interstitial

Anion and cation substitutions have been previously considered for n-type doping of Mg<sub>3</sub>Sb<sub>2</sub>. A less explored route is *via* insertion of cation interstitials. Here, we explore 4 different cations (Li, Zn, Cu, Be) that are small in size and can be possibly accommodated as interstitials in the Mg<sub>3</sub>Sb<sub>2</sub> crystal structure. We also report our experimental efforts of n-type doping with Li, which are in agreement with our theoretical predictions.

**Lithium, beryllium.** Due to its small size, it is expected that Li interstitials will undergo facile insertion into the  $Mg_3Sb_2$  structure. Indeed, Li interstitial (Li<sub>i</sub>) is predicted to have a much lower formation energy than Mg interstitials (Fig. 5a) and comparable in energy to substitutional dopants  $Se_{Sb}$  and  $Te_{Sb}$ . However, we find that acceptor defects,  $Li_{Mg(1)}$  and  $Li_{Mg(2)}$ , also have low formation energies. Consequently, the electrons generated by Li interstitials are strongly compensated by holes generated by the acceptor defects. We predict that the maximal free electron concentration (at Mg-rich and most Li-rich conditions) is lower (2.5  $\times$  10<sup>18</sup> cm<sup>-3</sup> at 900 K growth temperature) compared to self-doped  $Mg_3Sb_2$ , rendering Li an ineffective n-type dopant.

Unlike other cation dopants considered in this study, Li-rich conditions ( $\Delta\mu_{\rm Li}=0$  eV) cannot be achieved because of the formation of a Li-rich competing phase, Li\_3Sb (Section 5). However, this is not the limiting factor in n-type doping with Li. If the phase stability of Mg\_3Sb\_2 in the Mg–Sb–Li phase space could accommodate more Li-rich conditions, the formation energy of both Li\_i and Li\_{Mg} would be equally lower and the strong charge compensation would persist.

The energy differences between  $Li_{Mg}$  and  $Li_i$  are quite small, and thus the impact of Li doping is likely within the range of error within these calculations. To resolve this ambiguity, we synthesized  $Mg_3Sb_2$  under Mg-excess conditions at 873 K. The measured electron concentration in as-grown (Mg-rich) n-type  $Mg_3Sb_2$  is approximately 8.5  $\times$  10<sup>17</sup> cm<sup>-3</sup>. Doping with 2% Li suppresses the electron concentration by more than an order of magnitude to approximately 3.7  $\times$  10<sup>16</sup> cm<sup>-3</sup>. Our measurements are qualitatively consistent with the predicted defect energetics and suggest that the charge compensation may be more severe than predicted.

In case of monovalent cation dopants such as Li, substitutional  $D_{Mg}$  (where D is the dopant) can cause electron compensation, rendering the interstitial doping ineffective. In contrast, divalent cation dopants may be less sensitive to such compensation because  $D_{Mg}$  can be expected to be neutral. This is confirmed for Be doping, shown in Fig. S3 (ESI†), where the substitutional  $Be_{Mg}$ 

is neutral. However, Be is not an effective n-type dopant because of the high formation energy of Be interstitials.

Zinc, copper. We computationally assessed n-type doping via insertion of Zn and Cu interstitials as well as their corresponding substitutions on Mg and Sb sites (Fig. 5b and c). Copper interstitials are fairly common in other thermoelectric materials such as  $\text{Cu}_{2-x}\text{Se},^{24}$   $\text{Cu}_{14}\text{Sb}_4\text{S}_{13}.^{25}$  Zinc interstitials readily form in the thermoelectric material  $\beta\text{-Zn}_4\text{Sb}_3.^{26,27}$  Our defect calculations suggest that zinc is not an effective n-type dopant because the formation energy of Zn interstitials is fairly high compared to Mg interstitials (Fig. 5b). Unlike Li, Zn is isoelectronic with Mg; consequently, the lower-energy substitutional defect  $\text{Zn}_{\text{Mg}(2)}$  is charge neutral and does not cause charge compensation like  $\text{Li}_{\text{Mg}}$ .

The formation energy of Cu interstitials is slightly lower than that of Mg interstitials when  $E_{\rm F}$  is close to the conduction band minima (Fig. 5c) such that the maximal free electron concentration achieved (Mg-rich, Cu-rich conditions) is slightly higher than self-doping (4.9  $\times$  10<sup>18</sup> cm<sup>-3</sup> at 900 K, compared to 3.8  $\times$  10<sup>18</sup> cm<sup>-3</sup> in self-doped Mg<sub>3</sub>Sb<sub>2</sub>). The compensating defect Cu<sub>Mg(2)</sub> exhibits formation energy comparable to Cu interstitials near the conduction band minima. The +1 and -1 charge states of Cu<sub>i</sub> and Cu<sub>Mg</sub> suggests that Cu exists in +1 oxidation state in Mg<sub>3</sub>Sb<sub>2</sub>.

## 5 Discussion

The free carrier type (electrons or holes) and their concentrations in a semiconductor depend on the growth conditions, besides other factors. The predicted free electron concentrations as functions of temperature for self-doped and extrinsically-doped Mg<sub>3</sub>Sb<sub>2</sub> under Mg-rich and the most dopantrich conditions (as accommodated by Mg<sub>3</sub>Sb<sub>2</sub> phase stability) are shown in Fig. 6. The phase stability of Mg<sub>3</sub>Sb<sub>2</sub> represented in the binary Mg-Sb chemical potential space is bounded by

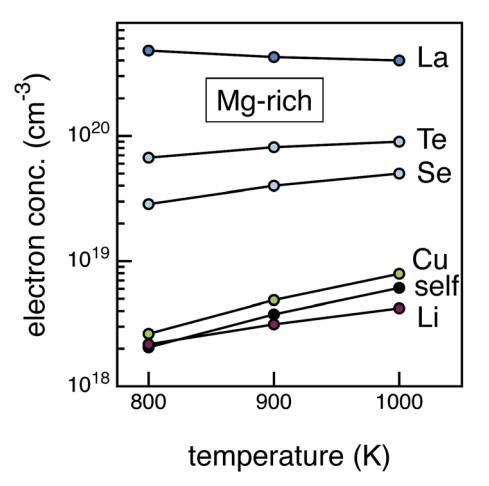


Fig. 6 Calculated free electron concentration as a function of temperature for self-doped and extrinsically doped Mg $_3$ Sb $_2$  under Mgrich ( $\Delta\mu_{Mg}=0$  eV) and the most dopant-rich conditions i.e., before secondary dopant-related phases start forming. For clarity, only 5 dopants (Li, Cu, Se, Te, La) are shown.

Mg-rich/Sb-poor conditions ( $\Delta \mu_{Mg} = 0$  eV) on one end and Mgpoor/Sb-rich conditions ( $\Delta \mu_{Sb} = 0$  eV) on the other. In the composition space, Mg-rich conditions correspond to Mg<sub>3</sub>Sb<sub>2</sub> in equilibrium with Mg, and Mg-poor conditions correspond to equilibrium with Sb. Mg<sub>3</sub>Sb<sub>2</sub> grown under Mg-poor conditions yield a p-type material3-5 while Mg3Sb2 grown under Mg-rich conditions is n-type.6-8 Therefore, to achieve the desired carrier type and concentrations in Mg<sub>3</sub>Sb<sub>2</sub>, specific regions of the phase stability region have to be accessed. In practice, this is accomplished in experiments by performing phase boundary mapping.<sup>6</sup> For instance, Mg-rich conditions ( $\Delta \mu_{\mathrm{Mg}} = 0$  eV) are accessed by growing Mg<sub>3</sub>Sb<sub>2</sub> with excess Mg such that trace amounts of Mg precipitates are present in equilibrium with  $Mg_3Sb_2$ .

When extrinsically doped, one must consider the stability of  $Mg_3Sb_2$  in the dopant-Mg-Sb ternary phase space.  $\Delta\mu_{dopant} =$ 0 eV corresponds to a dopant-rich condition or equilibrium with the dopant in elemental form. The range of dopant chemical potentials that can be accessed in the region of Mg<sub>3</sub>Sb<sub>2</sub> phase stability depends on the presence of competing phases and their stability. Here, we examine the phase stability of Mg<sub>3</sub>Sb<sub>2</sub> in the ternary dopant-Mg-Sb phase space for different dopants and the corresponding accessible range of dopant chemical potentials. The free carrier concentrations at the boundary of phase stability of Mg<sub>3</sub>Sb<sub>2</sub> and dopant-related competing phases are presented. We emphasize the importance of dopant phase boundary mapping to achieve the desired carrier type and concentrations. Finally, based on the predicted carrier concentrations, we derive general guidelines for the various doping strategies.

#### 5.1 Phase stability and carrier concentrations

The region of phase stability of Mg<sub>3</sub>Sb<sub>2</sub> in the ternary dopant-Mg-Sb phase space is presented in Fig. 7 for the 9 different dopants (Se, Br, I, La, Al, Ga, Li, Zn, Cu) considered in this study. The phase stability of Mg<sub>3</sub>Sb<sub>2</sub> in the Nb-Mg-Sb phase space is provided in Fig. S2 in the ESI.† The ternary phase space is represented by  $\Delta \mu_{\mathrm{Mg}}$  as the abscissa, ranging from Mg-rich condition ( $\Delta \mu_{\mathrm{Mg}} = 0$  eV) to Mg-poor ( $\Delta \mu_{\mathrm{Mg}} = -0.83$  eV). The abscissa also represents the corresponding  $\Delta\mu_{Sb}$ , ranging from -1.28 eV ( $\Delta \mu_{\rm Mg} = 0$  eV) to 0 eV ( $\Delta \mu_{\rm Mg} = -0.83$  eV). The ordinate, representing  $\Delta\mu_{\text{dopant}}$ , ranges from dopant-rich condition (0 eV) to dopant-poor (-3.5 eV). In principle, the dopant-poor condition can extend to  $-\infty$ , which corresponds to the condition where no dopant is present.

For each of the 9 dopants shown in Fig. 7, we have calculated the free carrier concentration (900 K) at the phase boundary between Mg<sub>3</sub>Sb<sub>2</sub> and the neighboring competing phases. The reasons for examining the carrier concentration at this boundary are two fold: (1) maximal carrier concentrations are achieved at this boundary, and (2) dopant phase boundary mapping can be performed in experiments by observing trace amounts of competing phases. The carrier concentrations are normalized by the free electron concentration in self-doped Mg<sub>3</sub>Sb<sub>2</sub> (3.8  $\times$  10<sup>18</sup> cm<sup>-3</sup>) grown under Mg-rich conditions (Fig. 2b) at 900 K. Electrons and holes are denoted by different colors.

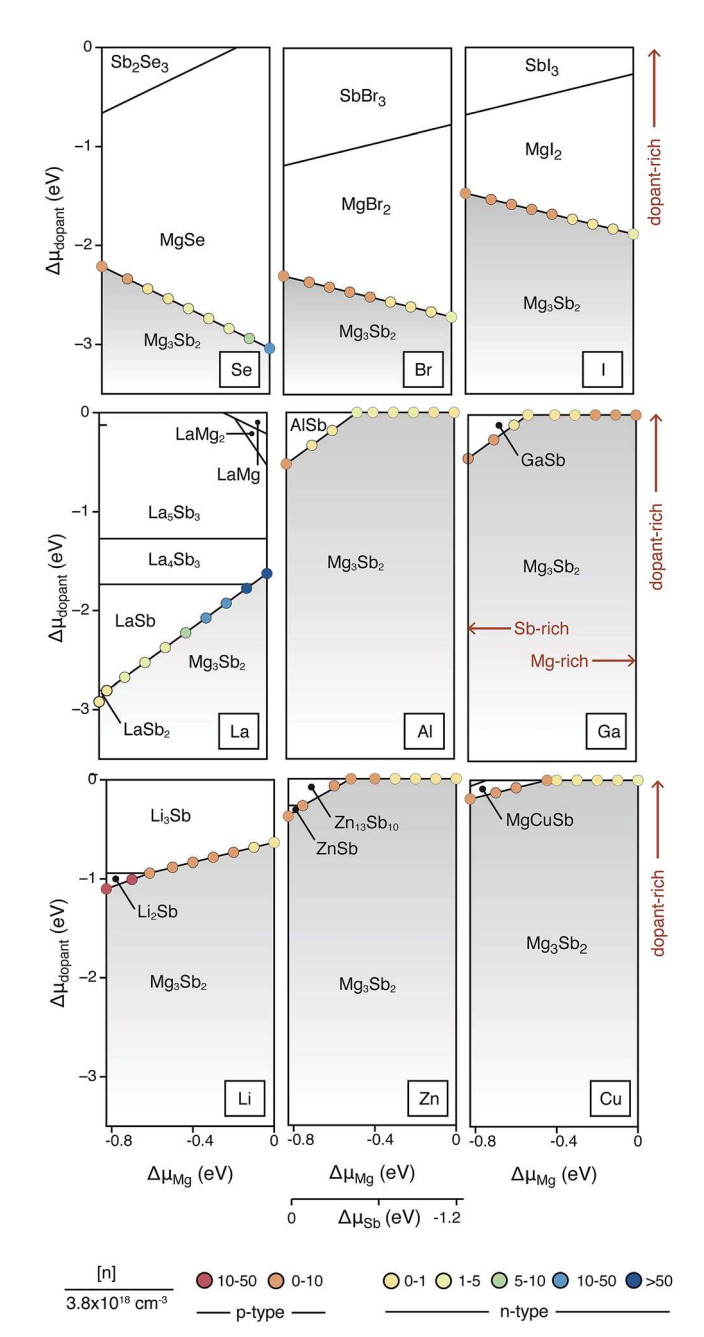


Fig. 7 Phase stability of Mg<sub>3</sub>Sb<sub>2</sub> in the ternary dopant-Mg-Sb chemical potential phase space. The shaded area represents the region of phase stability of  $Mg_3Sb_2$ . The x-axis is bounded by Mg-rich/ Sb-poor ( $\Delta \mu_{Mq} = 0$  eV,  $\Delta \mu_{Sb} = -1.28$  eV) and Mg-poor/Sb-rich ( $\Delta \mu_{Mq} = -1.28$  eV) -0.83 eV,  $\Delta \mu_{Sb} = 0$  eV) conditions. The y-axis denotes  $\Delta \mu_{dopant}$ , ranging from dopant-rich (0 eV) and below. The markers at the Mg<sub>3</sub>Sb<sub>2</sub> phase boundary are the free carrier concentrations calculated at 900 K, normalized by the free electron concentration in self-doped n-type  $Mg_3Sb_2$  grown under Mg-rich conditions (3.8  $\times$  10<sup>18</sup> cm<sup>-3</sup>). Red and orange markers denote free hole concentrations while other colors free electron concentrations.

For Se, Br, and I, the region of phase stability of Mg<sub>3</sub>Sb<sub>2</sub> is limited to fairly dopant-poor conditions due to the presence of stable Mg chalcogenide (MgSe) and Mg halide (MgBr<sub>2</sub>, MgI<sub>2</sub>) phases. In all three cases, the maximal electron concentration is

achieved at the boundary where Mg-rich ( $\Delta\mu_{\rm Mg}=0$  eV) conditions prevail. As discussed earlier, Se is an effective n-type dopant and therefore, the maximal free electron concentration is  $4\times 10^{19}$  cm<sup>-3</sup> at 900 K. Br and I are ineffective n-type dopants that only slightly increase free electron concentrations by a factor of  $\approx 1.2$  compared to self-doped n-type Mg<sub>3</sub>Sb<sub>2</sub>. There are several competing phases in the La-Mg-Sb

There are several competing phases in the La–Mg–Sb chemical space that limit the stability of  $Mg_3Sb_2$  to La-poor conditions, with maximum  $\Delta\mu_{\rm La}=-1.6$  eV (Fig. 7). Given the low formation energy of the substitutional  $La_{Mg(1)}$  (Fig. 3a), the maximal electron concentration of  $4\times10^{20}$  cm $^{-3}$  (at 900 K) is achieved under Mg-rich and the most La-rich conditions. The predicted maximal electron concentration is an order of magnitude larger than that achieved by Se doping (Fig. 6).

In case of Al and Ga, the dopant antimonides (AlSb, GaSb) are the only competing phases such that the region of phase stability of Mg<sub>3</sub>Sb<sub>2</sub> can access dopant-rich conditions ( $\Delta \mu_{A1.Ga}$  = 0 eV). Substitutional Al<sub>Sb</sub> and Ga<sub>Sb</sub> are strong charge (electron) compensating defects present in Al-doped and Ga-doped Mg<sub>3</sub>Sb<sub>2</sub>, respectively (Fig. 3a and b). As a result, the free carrier type and concentrations at the phase boundary exhibit interesting behavior. In Al-doped Mg<sub>3</sub>Sb<sub>2</sub>, the maximal electron concentration is not achieved under Mg- and Al-rich conditions  $(\Delta \mu_{A1} = 0 \text{ eV})$ . Instead, it is achieved under slightly Mg-poor/Sbrich conditions, where the formation energy of the compensating defect Al<sub>Sb</sub> is higher than under Mg-rich/Sb-poor conditions. Specifically, the maximal electron concentration is achieved at the triple point where Al, AlSb, and Mg<sub>3</sub>Sb<sub>2</sub> are in equilibrium. Since substitutional Gasb has a lower formation energy than Al<sub>Sb</sub> (Fig. 3), Mg<sub>3</sub>Sb<sub>2</sub> is doped p-type under Mg- and Ga-rich conditions ( $\Delta \mu_{Ga} = 0$  eV). Under slightly Mg-poor/Sbrich conditions, the carrier type changes - Mg<sub>3</sub>Sb<sub>2</sub> is doped ntype; the maximal free electron concentration is achieved at the triple point between Ga, GaSb, and Mg<sub>3</sub>Sb<sub>2</sub>. Whilst the effect of strong charge compensating defects on the free carrier concentrations in Mg<sub>3</sub>Sb<sub>2</sub> is subtle, the effect may be much more pronounced in other materials. In case of Nb (Fig. S2†), several competing Nb antimonide phases are present such that the most dopant-rich condition accessed by the phase stability of Mg<sub>3</sub>Sb<sub>2</sub> is limited to  $\Delta\mu_{\rm Nb} = -0.08$  eV. Nevertheless, given the high formation energy of substitutional Nb defects (Fig. S1†), the free carrier concentration remains unchanged compared to self-doped Mg<sub>3</sub>Sb<sub>2</sub>.

The presence of stable Li<sub>3</sub>Sb limits the most Li-rich condition to  $\Delta\mu_{\rm Li}=-0.63$  eV. The maximal free electron concentration is achieved at Mg-rich ( $\Delta\mu_{\rm Mg}=0$  eV) and most Li-rich condition ( $\Delta\mu_{\rm Li}=-0.63$  eV). Due to the strong charge compensation between the donor Li<sub>i</sub> and acceptor Li<sub>Mg</sub> (Fig. 5a), the maximal free electron concentration is lower than self-doped n-type Mg<sub>3</sub>Sb<sub>2</sub>. Interestingly, under Mg-poor/Sb-rich conditions ( $\Delta\mu_{\rm Sb}=0$  eV), the free hole concentration is 8.5 ×  $10^{19}$  cm<sup>-3</sup> due to the low formation energy of the acceptor Li<sub>Mg</sub> under those conditions; this suggest Li is a good p-type dopant under Sb-rich growth conditions. For Be, Zn and Cu, dopant-rich conditions ( $\Delta\mu_{\rm dopant}=0$  eV) are accessed by the phase stability of Mg<sub>3</sub>Sb<sub>2</sub>. However, due to the high formation energy of the Be and Zn interstitial, the free carrier concentration

remains unchanged compared to self-doped Mg<sub>3</sub>Sb<sub>2</sub>. The maximal free electron concentration for Cu doping, which is slightly higher than self-doped Mg<sub>3</sub>Sb<sub>2</sub> (Fig. 6), is achieved at Mg-rich and Cu-rich ( $\Delta\mu_{\rm Cu}=0$  eV) conditions.

We predict the free carrier concentrations from explicit defect calculations. Recently, Zhang et al.28 proposed guiding principles for n-type doping of Mg<sub>3</sub>Sb<sub>2</sub> based on the electronegativity difference  $(\Delta \chi)$  of the dopant (D) and Mg and Sb. According to the simple guiding principle, effective n-type doping on the anion site (Sb) is achieved for smaller dopant-Mg electronegativity differences  $(\Delta \chi_{D-Mg})$  and on the cation site, for smaller dopant-Sb electronegativity differences ( $\Delta \chi_{D-}$ <sub>Sb</sub>). Using the Pauling electronegativity scale,  $\Delta \chi_{D-Mg}$  is 1.24, 0.78, 1.65, and 1.35 for Se, Te, Br, and I, respectively. From our calculations, we find that I and Br are ineffective n-type dopants consistent with the guiding principle. However, our results suggest that the guiding principle cannot be extended to the cation site doping. For instance,  $\Delta \chi_{\text{La-Sb}}$  is 0.95, which is much larger than  $\Delta \chi_{\text{Ga-Sb}}$  (0.24), and  $\Delta \chi_{\text{Cu-Sb}}$  (0.15). While useful, the guiding principle28 simply assumes substitutional doping on the intended lattice site. Explicit defect calculations presented in this work reveal that cation site doping is more complex. For example, strong charge compensation may occur due to unexpected, facile substitution on the anion site, as in the case of Ga doping. Explicit defect calculations, in lieu of guiding principles, are further necessitated for interstitial doping. Again, we observe the significant role of charge compensation even for interstitial doping *e.g.* Li doping ( $\Delta \chi_{\text{Li-Sb}} = 1.07$ ).

## 6 Conclusions

In this work, we have computationally assessed three different n-type doping strategies for Mg<sub>3</sub>Sb<sub>2</sub>, including anion substitution, cation substitution, and interstitial insertion. Out of the 11 possible dopants considered, Se (and previously Te) is found to be the most effective for anion substitution and La for cation substitution. Interstitial doping with Li, Zn, Cu, and Be is found to be ineffective for n-type doping; however, Li is identified as a good p-type dopant. The following guidelines emerge from this study for the different n-type doping strategies:

- Anion substitution: maximal electron concentration is achieved under Mg-rich and most dopant-rich conditions accessed by the phase stability of Mg<sub>3</sub>Sb<sub>2</sub>.
- Cation substitution: due to the presence of low formation energy electron-compensating defects, the maximal electron concentration is achieved under slightly Mg-poor/Sb-rich conditions. If the compensating defects have high formation energy, the maximal electron concentration is achieved under Mg-rich and most dopant-rich conditions. Of all the elements considered, La is found to be the most effective n-type dopant and Mg substitution the most effective doping strategy in terms of the achievable electron concentrations.
- ullet Interstitial insertion: cation interstitials maximize the electron concentration under Mg-rich and most dopant-rich conditions. In case of monovalent cation dopants, electron compensation by low formation energy substitutional  $D_{\rm Mg}$ , where D is the dopant, can be suppressed under Mg-rich

conditions. In contrast, divalent cation dopants are less sensitive to this concern because  $D_{Mg}$  can be expected to be neutral.

Traditionally, semiconductors are doped to enhance the free carrier concentrations, as in the case of Mg<sub>3</sub>Sb<sub>2</sub>. However, in degenerately self-doped semiconductors, there may be a need to lower the free carrier concentration in order to maximize zT. This can be achieved by doping that introduces the desired charge compensating defects combined with dopant phase boundary mapping.

## Conflicts of interest

The authors declare no conflict of interests.

## Acknowledgements

We thank G. Jeffrey Snyder for fruitful discussions. We acknowledge support from NSF DMR program, grant no. 1729594. The research was performed using computational resources sponsored by the Department of Energy's Office of Energy Efficiency and Renewable Energy and located at the NREL.

## References

- 1 G. J. Snyder and E. S. Toberer, Nat. Mater., 2008, 7, 105.
- 2 P. Gorai, V. Stevanovic and E. S. Toberer, Nat. Rev. Mater., 2017, 2, 1-16.
- 3 V. Ponnambalam and D. T. Morelli, J. Electron. Mater., 2013, 42, 1307-1312.
- 4 C. L. Condron, S. M. Kauzlarich, F. Gascoin and G. J. Snyder, J. Solid State Chem., 2006, 179, 2252-2257.
- 5 A. Bhardwaj and D. K. Misra, RSC Adv., 2014, 4, 34552-34560.
- 6 S. Ohno, K. Imasato, S. Anand, H. Tamaki, S. D. Kang, P. Gorai, H. K. Sato, E. S. Toberer, T. Kanno and G. J. Snyder, Joule, 2017, 2, 141.
- 7 H. Tamaki, H. K. Sato and T. Kanno, Adv. Mater., 2016, 28, 10182-10187.
- 8 J. Zhang, L. Song, A. Mamakhel, M. R. V. Jørgensen and B. B. Iversen, Chem. Mater., 2017, 29, 5371-5383.
- 9 J. Zhang, L. Song, S. H. Pedersen, H. Yin, L. T. Hung and B. B. Iversen, Nat. Commun., 2017, 8, 1-8.
- 10 J. Yan, P. Gorai, B. Ortiz, S. Miller, S. A. Barnett, T. Mason, V. Stevanovic and E. S. Toberer, Energy Environ. Sci., 2015, 8, 983.

- 11 H. Peng, D. O. Scanlon, V. Stevanovic, J. Vidal, G. W. Watson and S. Lany, Phys. Rev. B: Condens. Matter Mater. Phys., 2013, 88, 115201.
- 12 S. Lany and A. Zunger, Phys. Rev. B: Condens. Matter Mater. Phys., 2008, 78, 235104.
- 13 J. P. Perdew, K. Burke and M. Ernzerhof, Phys. Rev. Lett., 1996, 77, 3865.
- 14 G. Kresse and J. Furthmüller, Phys. Rev. B: Condens. Matter Mater. Phys., 1996, 54, 11169.
- 15 B. Ortiz, P. Gorai, V. S. Stevanović and E. S. Toberer, Chem. Mater., 2017, 29, 4523.
- 16 V. Stevanović, S. Lany, X. Zhang and A. Zunger, Phys. Rev. B: Condens. Matter Mater. Phys., 2012, 85, 115104.
- 17 A. Goyal, P. Gorai, H. Peng, S. Lany and V. S. Stevanović, Comput. Mater. Sci., 2016, 130, 1.
- 18 G. S. Pomrehn, A. Zevalkink, W. G. Zeier, A. van de Walle and G. J. Snyder, Angew. Chem., 2014, 53, 3422-3426.
- 19 L. Bjerg, G. K. H. Madsen and B. B. Iversen, Chem. Mater., 2012, 24, 2111-2116.
- 20 E. S. Toberer, A. Zevalkink, N. Crisosto and G. J. Snyder, Adv. Funct. Mater., 2010, 20, 4375-4380.
- 21 J. Mao, J. Shuai, S. Song, Y. Wu, R. Dally, J. Zhou, Z. Liu, J. Sun, Q. Zhang, C. dela Cruz, S. Wilson, Y. Pei, D. J. Singh, G. Chen, C.-W. Chu and Z. Ren, Proc. Natl. Acad. Sci. U. S. A., 2017, 114, 10548-10553.
- 22 J. Shuai, J. Mao, S. Song, Q. Zhu, J. Sun, Y. Wang, R. He, J. Zhou, G. Chen, D. J. Singh and Z. Ren, Energy Environ. Sci., 2017, 10, 799-807.
- 23 J. ichi Tani, M. Takahashi and H. Kido, Phys. B, 2010, 405, 4219-4225.
- 24 H. Liu, F. Xu, L. Zhang, W. Zhang, L. Chen, Q. Li, C. Uher, T. Day and G. J. Snyder, Nat. Mater., 2012, 11, 422-425.
- 25 D. P. Weller, D. L. Stevens, G. E. Kunkel, A. M. Ochs, C. F. Holder, D. T. Morelli and M. E. Anderson, Chem. Mater., 2017, 29, 1656-1664.
- 26 E. S. Toberer, K. A. Sasaki, C. R. I. Chisholm, S. M. Haile, W. A. Goddard and G. J. Snyder, Phys. Status Solidi, 2007, 1, 253-255.
- 27 F. Cargnoni, E. Nishibori, P. Rabiller, L. Bertini, G. J. Snyder, M. Christensen, C. Gatti and B. B. Iversen, Chem.-Eur. J., 2004, 10, 3861-3870.
- 28 J. Zhang, L. Song, K. A. Borup, M. R. V. Jorgensen and B. B. Iversen, Adv. Energy Mater., 2018, 8, 1702776.